



# Acidity-activity correlation over bimetallic iron-based ZSM-5 catalysts during selective catalytic reduction of NO by NH<sub>3</sub>



Sayedeh Halima Begum<sup>a,b,1</sup>, Chin-Te Hung<sup>a</sup>, Yit-Tsong Chen<sup>a,b</sup>, Shing-Jong Huang<sup>c</sup>, Pei-Hao Wu<sup>a</sup>, Xiaoxiang Han<sup>d,\*\*</sup>, Shang-Bin Liu<sup>a,e,\*</sup>

<sup>a</sup> Institute of Atomic and Molecular Sciences, Academic Sinica, Taipei 10617, Taiwan

<sup>b</sup> Department of Chemistry, National Taiwan University, Taipei 10617, Taiwan

<sup>c</sup> Instrumentation Center, National Taiwan University, Taipei 10617, Taiwan

<sup>d</sup> Department of Applied Chemistry, Zhejiang Gongshang University, Hangzhou 310035, China

<sup>e</sup> Department of Chemistry, National Taiwan Normal University, Taipei 11677, Taiwan

## ARTICLE INFO

### Article history:

Received 19 May 2016

Received in revised form 18 July 2016

Accepted 20 July 2016

Available online 22 July 2016

### Keywords:

Bimetallic Fe-based zeolite

Acidity

NO<sub>x</sub> reduction

NH<sub>3</sub>-SCR

<sup>31</sup>P MAS NMR

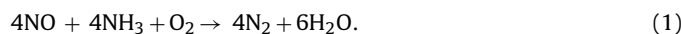
## ABSTRACT

The effect of acidic properties over a series of Lanthanide metal incorporated Fe-based H-ZSM-5 (Si/Al = 15) catalysts on catalytic activity during selective catalytic reduction (SCR) of NO by NH<sub>3</sub> was investigated. Various mono- ( $M_1$ -ZSM-5;  $M_1$  = Fe, Ce, Pr, Nd, and Sm) and bimetallic ( $M_2$ Fe-ZSM-5;  $M_2$  = Ce, Pr, Nd, and Sm) catalysts were prepared and their physicochemical properties were characterized by a variety of analytical and spectroscopic techniques. In particular, their acidic properties were studied by different molecular probe techniques, including the conventional ammonia-TPD and pyridine-IR methods, as well as solid-state <sup>31</sup>P MAS NMR of adsorbed trimethylphosphine oxide (TMPO). Among various catalysts examined, the CeFe-ZSM-5 catalyst was found to exhibit an optimal NO conversion exceeding 95% over a temperature range of 300–500 °C (WHSV = 68,000 cm<sup>3</sup> g<sup>-1</sup> h<sup>-1</sup>). The superior SCR activity observed for the bimetallic Fe-based catalysts is attributed to the synergistic effect from the Brønsted acidity of the MFI zeolite and strong Lewis acidity induced by the incorporated active metal ion species, particularly when incorporated with a secondary Lanthanide metal ion.

© 2016 Elsevier B.V. All rights reserved.

## 1. Introduction

Nitrogen oxides (NO<sub>x</sub>;  $x = 1, 2$ ), namely nitric oxide (NO) and nitrogen dioxide (NO<sub>2</sub>), are hazardous air pollutants, mostly emitting from both mobile and stationary sources. The state-of-the-art DeNO<sub>x</sub> process technology for efficient removal of NO invokes the standard selective catalytic reduction (SCR) of NO by ammonia [1,2]:



Microporous zeolites have been widely exploited as solid acid catalysts for the SCR DeNO<sub>x</sub> process owing to their unique prop-

erties such as well-defined pore structures, high surface areas (*ca.* 500–800 m<sup>2</sup> g<sup>-1</sup>), thermal stability (up to *ca.* 800 °C), and desirable acidity [3]. It has been revealed that the framework of microporous zeolites plays an important role during the SCR of NO and that the incorporation of non-reducible Al<sup>3+</sup> ions onto H-ZSM-5 zeolite tends to enhance the acidity of the catalyst desirable for the SCR reaction [4]. Moreover, in terms of reducing the NO<sub>x</sub> emission from mobile sources, such as automobile diesel engines, iron (Fe)-based zeolites are most desirable catalysts owing to their high activity and durability [5–11]. The advantage of employing metal-based zeolites for the SCR process is that NO must be first oxidized to form NO<sub>2</sub>, which is the rate-determining step of the reaction. For the Fe-based zeolite catalyst, the incorporated Fe metals act as the primary active centers for the formation of NO<sub>2</sub>, while the SCR reaction invokes acid sites located in pore channels of the zeolite. While NO<sub>2</sub> is anticipated to be consumed immediately after its formation during SCR processes, further reduction of NO<sub>x</sub> with NH<sub>3</sub> should be closely related to the incorporated Fe, whose presences greatly affect the detailed acid features (e.g., type, concentration, and strength of acid sites) of the acid catalyst.

\* Corresponding author at: Institute of Atomic and Molecular Sciences, Academic Sinica, Taipei 10617, Taiwan.

\*\* Corresponding author.

E-mail addresses: [hxx74@126.com](mailto:hxx74@126.com) (X. Han), [sbliu@sinica.edu.tw](mailto:sbliu@sinica.edu.tw), [sbliu.iams@gmail.com](mailto:sbliu.iams@gmail.com) (S.-B. Liu).

<sup>1</sup> Present address: Department of Chemistry, University of Chittagong, Chittagong 4331, Bangladesh.

Nonetheless, regardless of the R&D attention drawn for Fe-based zeolite catalysts (particularly Fe-ZSM-5) in the activation of  $\text{NO}_x$ , the active sites invoked for the superior catalytic performance during the SCR reaction and the role of acidity of the supported catalyst remain uncertain [12]. In addition, while the Fe-ZSM-5 catalyst may be prepared by a variety of facile methods, leading to the formations of  $\text{Fe}_3\text{O}_4$  nanoclusters and/or isolated Fe cations, the nature, concentration, and roles of these Fe active sites remain to be understood [13]. Boroń et al. [14] reported a series of Fe-containing zeolites prepared by different methods. The authors attributed the variations in catalytic activities during NO reduction due to the presence of pseudo-tetrahedral  $\text{Fe}^{3+}$  species. It was hypothesized that the strength and distribution of Brønsted and Lewis acidic sites in H-ZSM-5 may be altered upon incorporation of the Fe metal species onto the zeolite catalyst, which would in turn shifting the overall catalytic activity towards lower temperatures [13]. However, the authors proposed that the influence of Brønsted acidity is less obvious during  $\text{NH}_3$ -SCR. Brandenberger et al. [12] reported that the presence of Brønsted acidity in the zeolite catalyst (hereafter denoted by 'Z') is vital during the SCR of  $\text{NO}_x$  in  $\text{NH}_3$ ; the formation of ammonium ions tends to further react with the surface  $\text{NO}_x$  species to form active complex, such as  $[(\text{NH}_4)_x\text{NO}_2](x=1, 2)$ , leading to the yields of  $\text{N}_2$  and  $\text{H}_2\text{O}$  [12,15–23]. On the other hand, Peña et al. [24] pointed out that the coexistence of Brønsted and Lewis acidic sites is essential for the SCR of NO. The existence of Brønsted-Lewis acid synergy during  $\text{NH}_3$ -SCR has been proposed over the Mn/Al-SBA-15 catalyst by Liang and co-workers [25]. However, the effect of Brønsted and/or Lewis acidity during the De $\text{NO}_x$  process is still lacking, mainly due to inadequate information on detailed acid features.

An alternative approach for promoting the SCR activity of the Fe-based catalyst is through the incorporation of a secondary metal species. Recently, a notable increase in relevant field was evident [5,26–30]. For example, Long and Yang [5] introduced cerium (Ce) as the secondary metal onto the Fe-ZSM-5 catalyst and found that the presence of Ce readily helped to improve the activity and stability of the catalyst while in the presence of  $\text{H}_2\text{O}$  and  $\text{SO}_2$ . As one of the key ingredients in automotive three-way catalysts, the redox cycle prevailing between the trivalent and tetravalent oxidation states of Ce metal ions readily helps to promote the oxygen storage capability of the catalyst during the reaction. However, unlike bimetallic CeFe-ZSM-5 catalyst, the monometallic Ce-ZSM-5 showed inferior SCR activity and stability owing to the demand for a higher reduction temperature (above 700 °C) and vulnerability for sintering [29].

In view of the existing debates on the nature of active sites and the role of acidity during  $\text{NH}_3$ -SCR over the Fe-based mono- and bimetallic MFI zeolite catalysts, the objective of this study aims to resolve these crucial issues in a more inclusive manner. Herein, a series of Fe-based H-ZSM-5 zeolite catalysts incorporated with different secondary Lanthanide metals (Ce, Pr, Nd, and Sm) were prepared by using the reflux method. Their physico-chemical properties were characterized by a variety of analytical and spectroscopic techniques. In particular, their acidic properties were examined by different molecular probe techniques, namely  $\text{NH}_3$ -TPD, pyridine-IR [31,32], and  $^{31}\text{P}$  MAS NMR of the adsorbed trimethylphosphine oxide (TMPO) probe molecule [33–35]. As will be shown later that the latter  $^{31}\text{P}$  TMPO NMR approach readily affords simultaneous quantitative determination of detailed acid features, viz. type, concentration, and strength of acid sites for various mono- and bimetallic Fe-based ZSM-5 catalysts before and after the  $\text{NH}_3$ -SCR reaction. To the best of our knowledge, this is the first study to directly correlate the SCR activity of the Fe-based supported zeolites with detailed variations of acidic features possessed by the catalysts.

## 2. Experimental

### 2.1. Catalyst preparation

Fe-based mono- and bimetallic ZSM-5 catalysts incorporated with various Lanthanide metals ( $M = \text{Ce}, \text{Pr}, \text{Nd}$ , and  $\text{Sm}$ ) were prepared by using the reflux method. The preparation of monometallic  $M_1\text{-Z}$  ( $M_1 = \text{Fe}, \text{Ce}, \text{Pr}, \text{Nd}$ , and  $\text{Sm}$ ;  $Z = \text{ZSM-5 zeolite}$ ) catalysts were carried out by first dispersing a known amount of the respective metal precursor, namely iron acetylacetone, cerium nitrate, praseodymium nitrate, neodymium nitrate, or samarium nitrate (Aldrich, 99.99%) in 80 mL acetonitrile, then mix with 5 g of H-ZSM-5 zeolite ( $\text{Si}/\text{Al} = 15$ ; surface area ca. 375 m<sup>2</sup> g<sup>-1</sup>; Zeolyst) at 80 °C under vigorous stirring in a refluxing flask for 24 h [31]. The resultant mixture solutions were filtered, dried (at 110 °C overnight), then subjected to calcination treatment in air at 600 °C for 5 h. Similar method was exploited for the preparation of bimetallic Fe-based  $M_2\text{-Fe-Z}$  ( $M_2 = \text{Ce}, \text{Pr}, \text{Nd}$ , and  $\text{Sm}$ ) catalysts, the only difference being the simultaneously dispersion of the primary (Fe) and the secondary ( $M_2$ ) metal acetylacetone precursors in acetonitrile prior to mixing with the H-ZSM-5 zeolite. A typical metal content of ca. 5 wt% was used for both  $M_1$  and  $M_2$  during the preparation of various mono- ( $M_1\text{-Z}$ ) and bimetallic ( $M_2\text{-Fe-Z}$ ) catalysts.

### 2.2. SCR performance

The SCR of NO by  $\text{NH}_3$  were performed on a home-built fixed-bed quartz tube reactor (inner diameter 7 mm) under atmospheric pressure. The reaction temperature was manipulated and monitored by a programmable temperature controller. Prior to each run, ca. 0.1 g of the catalyst was first pretreated at 500 °C in air for 1 h. Reactions were carried out under the conditions:  $[\text{NO}] = [\text{NH}_3] = 500 \text{ ppm}$ ,  $[\text{O}_2] = 2.9 \text{ vol\%}$ , balance  $\text{N}_2$ ,  $\text{GHSV} = 68,000 \text{ cm}^3 \text{ g}^{-1} \text{ h}^{-1}$ , and total flow rate 350 mL min<sup>-1</sup>. The concentrations of NO and  $\text{NO}_2$  were simultaneously monitored by an on-line chemiluminescence  $\text{NO}_x$  analyzer (Thermo Scientific, Model 42i-HL). Although the apparatus available was unable to monitor the  $\text{N}_2\text{O}$  yield, it is anticipated that its concentration should be negligible over the temperature range (100–500 °C) examined [5]. Moreover, the  $\text{NO}_2$  concentration detected during SCR was typically less than 1 ppm. In this context, the NO selectivity to  $\text{N}_2$  observed for various catalysts examined herein should be in close resemblance to their corresponding NO conversion, which was obtained from the difference in  $\text{NO}_x$  concentrations before and after the SCR reaction under steady-state condition (ca. 1 h) at each temperature.

### 2.3. Characterization methods

The chemical compositions of various catalysts were obtained by inductively coupled plasma mass/atomic emission spectrometry (ICP-MS/AES; PE/Sciex ELAN 6100 DRC and EVISA) as well as X-ray fluorescence (XRF; Horiba XGT-7000 V) techniques. All catalysts were characterized by powdered X-ray diffraction (XRD) using a PANalytical (X' Pert PRO) diffractometer with  $\text{CuK}\alpha$  radiation ( $\lambda = 0.15418 \text{ nm}$ ) at 45 kV and 40 mA. The XRD diffractograms were recorded over a  $2\theta$  range of 20–80° at a 0.02° interval and a counting time of 4.45 s. Physisorption of Ar and  $\text{N}_2$  was performed at 77 K on a Quantachrome Autosorb-1 apparatus. Prior to each adsorption measurement, the sample was subjected to an evacuation treatment at 350 °C for 16 h. The microporous volumes of various samples were obtained from the *t*-plot analyses. The Brunauer-Emmett-Teller (BET) method was used to derive the total surface areas of the samples. Transmission electron microscopy (TEM) experiments were operated at 200 kV on a JEOL JEM-2100f apparatus, which was equipped with an Oxford INCA

energy-dispersive X-ray (EDX) spectrometer, electron energy loss spectroscopy (EELS), and a charge coupled device (CCD) camera. Sample was mounted on holey carbon-coated copper grids. X-ray photoelectron spectroscopy (XPS) studies were carried out on a Perkin-Elmer PHI 5400 ESCA system at RT under  $10^{-8}$ – $10^{-9}$  Torr using MgK $\alpha$  radiation. Binding energy of Fe $_{2p}$  was calibrated relative to the carbon impurity with C $_{1s}$  at 284.5 eV. Temperature programmed desorption of ammonia (NH $_3$ -TPD) measurements were carried out on a Micromeritics AutoChem 2920 apparatus using a thermal conductivity detector (TCD). Prior to the measurement, the powdered sample (*ca.* 100 mg) was pretreated by ramping the temperature from ambient to 600 °C (ramp rate 15 °C min $^{-1}$ ) under flowing He (50 mL min $^{-1}$ ), then, kept at the final temperature for 2 h. While the sample was stabilized at 100 °C, it was dosed with 15% NH $_3$ /He (50 mL min $^{-1}$ ) for 15 min, then, flushing with He (50 mL min $^{-1}$ ) for 15 min to remove the physisorbed NH $_3$ , followed by lowering the temperature to 50 °C till reaching a stable condition, as indicated by the TCD. Finally, the NH $_3$ -TPD profile was recorded by ramping the temperature from 50 to 600 °C at a rate of 10 °C min $^{-1}$ . Pyridine-infrared (IR) spectra of various Fe-based zeolite catalysts were measured by using a Fourier-transform infrared (FT-IR) spectrometer (Bruker IFS 28) equipped with a variable temperature vacuum chamber and CaF $_2$  windows, which is connected to gas inlet and outlet (vacuum manifold) ports. Prior to pyridine adsorption, powder zeolite catalyst (*ca.* 15 mg) was pressed into a pellet (12 mm in diameter), then, pretreated at 400 °C for 2 h under vacuum, followed by cooling the sample to 100 °C for the adsorption of pyridine for *ca.* 1 h. Subsequently, the physisorbed pyridine was removed by evacuation at 100 °C overnight. All IR spectra were recorded at different temperatures (100–400 °C) with a total of 100 scans and a resolution of 4 cm $^{-1}$ . The relative concentration of Brønsted vs Lewis acidic sites was determined by the ratio of the corresponding areas of the absorption bands at 1545 and 1450 cm $^{-1}$ , respectively [32].

All solid-state nuclear magnetic resonance (NMR) experiments were carried out on a Bruker-Biospin AVANCE III 500 MHz NMR spectrometer using a 4 mm double resonance magic-angle spinning (MAS) probehead. The Larmor frequencies for the  $^{31}\text{P}$  and  $^{27}\text{Al}$  nuclei are 202.46 and 130.32 MHz, respectively. All free induction decay (FID) signals were acquired using a single-pulse sequence under a sample spinning rate of 12 kHz. The excitation pulse for  $^{31}\text{P}$  and  $^{27}\text{Al}$  was 1.5 (*ca.*  $\pi/6$  pulse) and 1.0  $\mu\text{s}$  (*ca.*  $\pi/12$  pulse) and the corresponding recycle delay was 10.0 and 0.5 s, respectively. The chemical shifts of  $^{31}\text{P}$  and  $^{27}\text{Al}$  were referenced to 85% H $_3\text{PO}_4$  and 1 M Al(NO $_3$ ) $_3$  aqueous solutions, respectively. It has been demonstrated that detailed acidic features, namely the type (Brønsted vs Lewis), strength, concentration (amount), and location (intra- vs extra-crystalline) of the acidic sites may be inferred from the  $^{31}\text{P}$  MAS NMR of the adsorbed trialkylphosphine oxide (R $_3$ PO) probe molecules [33–35]. It has been shown that a linear correlation between the observed  $^{31}\text{P}$  NMR chemical shifts ( $\delta^{31}\text{P}$ ) with the strength of acidic sites may be inferred [34–37]. Herein, we have chosen to utilize trimethylphosphine oxide (TMPO) as the probe molecule, which is known as the  $^{31}\text{P}$  TMPO NMR approach for acidity characterization. In this context, prior to the adsorption of TMPO probe molecule, the catalyst was first subjected to a thorough dehydration treatment at 350 °C for 48 h under vacuum (<10 $^{-5}$  Torr). Subsequently, a known amount of TMPO dissolved in anhydrous CH $_2\text{Cl}_2$  was introduced into a vessel containing the dehydrated solid sample in a N $_2$  glove box, followed by the removal of the CH $_2\text{Cl}_2$  solvent under a vacuum manifold at 50 °C. To ensure a uniform adsorption of adsorbate probe molecules in the pores/channels of the porous adsorbents, the sealed sample vessel was further subjected to thermal treatment at *ca.* 150 °C (note that the melting point of TMPO is *ca.* 140 °C) for at least 1 h. Finally, the sealed sample vessel was placed in a N $_2$  glove box where the TMPO-

loaded sample was transferred into a MAS rotor, and then sealed by a gas-tight Kel-F cap.

### 3. Results and discussion

#### 3.1. Catalyst structural property

All mono- (M $_1$ -Z; M $_1$  = Fe, Ce, Pr, Nd, and Sm) and bimetallic M $_2$ Fe-Z (M $_2$  = Ce, Pr, Nd, and Sm) catalysts exhibited the anticipated XRD patterns with characteristics peaks of MFI skeleton, nearly identical to that of the pristine H-ZSM-5 (see Figs. S1 and S2 of the Supporting information; hereafter denoted as SI†), indicating that ordered framework structures of the zeolite remain intact even after the incorporation of mono- and bimetallic species and the subsequent calcination treatment. Moreover, no detectable traces of characteristic XRD peaks responsible for bulk iron oxides (e.g., Fe $_{2\text{O}_3}$  or Fe $_{3\text{O}_4}$ ; corresponding to  $2\theta = 33.2$ , 35.6, and 49.5°) were observed in various mono-(M $_1$ -Z) and bi-metal (M $_2$ Fe-Z) catalysts (Fig. S2; SI†), suggesting that the metal oxides so incorporated are highly dispersed on the supported catalysts; their particle sizes may be too small to be detected. The structural integrity of the pristine H-ZSM-5 was also confirmed by solid-state  $^{27}\text{Al}$  MAS NMR, which revealed multiple resonances, including a primary peak at *ca.* 55 ppm, a weak shouldering peak at *ca.* 30 ppm, as well as a weak peak at *ca.* 0 ppm (Fig. S3a; SI†). The  $^{27}\text{Al}$  resonances at *ca.* 55 and 0 ppm may be unambiguously attributed to tetrahedral- and octahedral-coordinated Al species in the zeolite framework [38,39]. Thus, it is indicative that the pristine H-ZSM-5 possesses primarily aluminosilicates with tetrahedral framework and only a relatively smaller amount of extra-framework Al (EFAl) species are present in the zeolite sample [40,41]. The weak signal appeared at *ca.* 30.0 ppm may be ascribed due to the presence of distorted tetrahedral- or penta-coordinated EFAl species [42–44]. Upon loading metal species onto the H-ZSM-5, the  $^{27}\text{Al}$  MAS NMR spectra observed for the mono- (Fig. S3; SI†) and bimetallic (Fig. S4; SI†) remained practically unchanged, indicating the retention of MFI framework structure.

It is noted that while a typical M $_1$  and M $_2$  metal contents of *ca.* 5 wt% was used during preparation of various mono- (M $_1$ -Z) and bimetallic (M $_2$ Fe-Z) catalysts (*vide supra*), the actual metal concentrations somewhat deviate from the nominal value due to leaching during the washing/filtration treatments. To afford more reliable data for metal loadings, XRF technique was exploited in addition to the conventional elemental analysis techniques, such as ICP-MS/AES. Moreover, the reason for performing additional XRF analyses is that some of the Lanthanide metals cannot be completely dissolved in the acid solvent during the ICP-MS/AES measurements. On the basis of these analyses, most M $_1$ -Z and M $_2$ Fe-Z catalysts appear to have similar mono- and bimetallic contents of *ca.* 0.5–0.7 wt% (see Table 1).

Nevertheless, as will be shown later that the M $_1$ -Z and M $_2$ Fe-Z catalysts so prepared exhibit better SCR performances compared to the pristine H-ZSM-5, revealing that the metal species are highly dispersed on the zeolite support. The BET surface area (S $_{\text{BET}}$ ) obtained from N $_2$  adsorption/desorption isotherms of assorted mono- and bimetallic catalysts provide additional supports to the above notions. As depicted in Table 1, the BET surface area obtained from the desorption branch of the isotherm (Fig. S5; SI†) observed for the Fe-Z and CeFe-Z samples was 348 and 310 m $^2$  g $^{-1}$ , respectively; both slightly lower than that of the pristine H-ZSM-5 (374 m $^2$  g $^{-1}$ ). The marginal decreases (*ca.* 20%) in surface areas of the metal-incorporated catalysts compared to the pristine ZSM-5 support indicates that the incorporated Fe and the secondary Lanthanide metal (Ce) are highly dispersed on the surfaces of the zeolite, in consistent with the XRD results. This notion is further jus-

**Table 1**

Metal contents, textural parameters, and acidic properties of the pristine H-ZSM-5 (Si/Al = 15), Fe-ZSM-5, and bimetallic M<sub>2</sub>Fe-ZSM-5 (M<sub>2</sub> = Ce, Pr, Nd, and Sm) catalysts<sup>a</sup>.

Catalyst	Metal content (wt%)		$S_{BET}(\text{m}^2 \text{ g}^{-1})$	$V_{\text{tot}}(\text{cm}^3 \text{ g}^{-1})$	Amount NH <sub>3</sub> desorbed (mmol/g)	
	Fe	M <sub>2</sub>			177 °C	380 °C
H-ZSM-5	—	—	374	0.21	1.10	0.69
Fe-Z	0.5	—	348	0.15	3.36	1.59
CeFe-Z	0.7	0.5	310	0.28	3.86	1.74
PrFe-Z	0.6	0.5	ND	ND	3.25	1.55
NdFe-Z	0.7	0.6	ND	ND	3.19	1.43
SmFe-Z	0.7	0.6	ND	ND	3.19	1.43

<sup>a</sup> Metal content determined by XRF elemental analysis technique. ND = not determined.

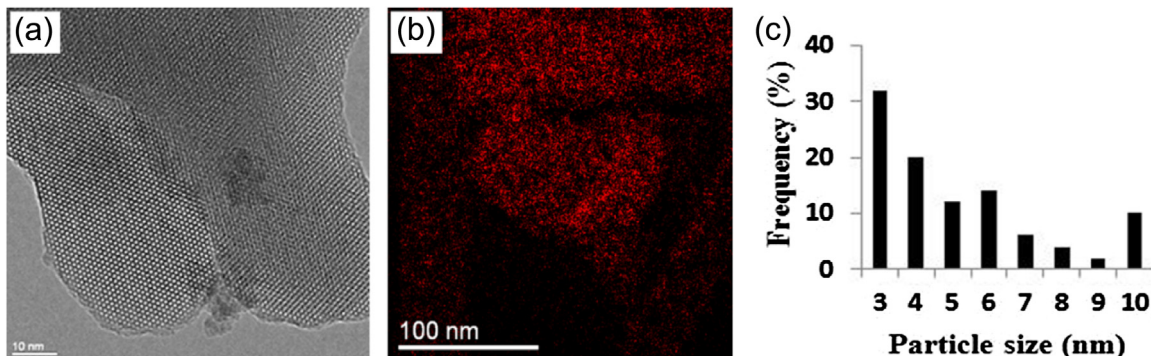


**Fig. 1.** (a) FE-TEM image, (b) EELS mapping of Fe, and (c) particle size distribution histogram of the Fe-Z catalyst.

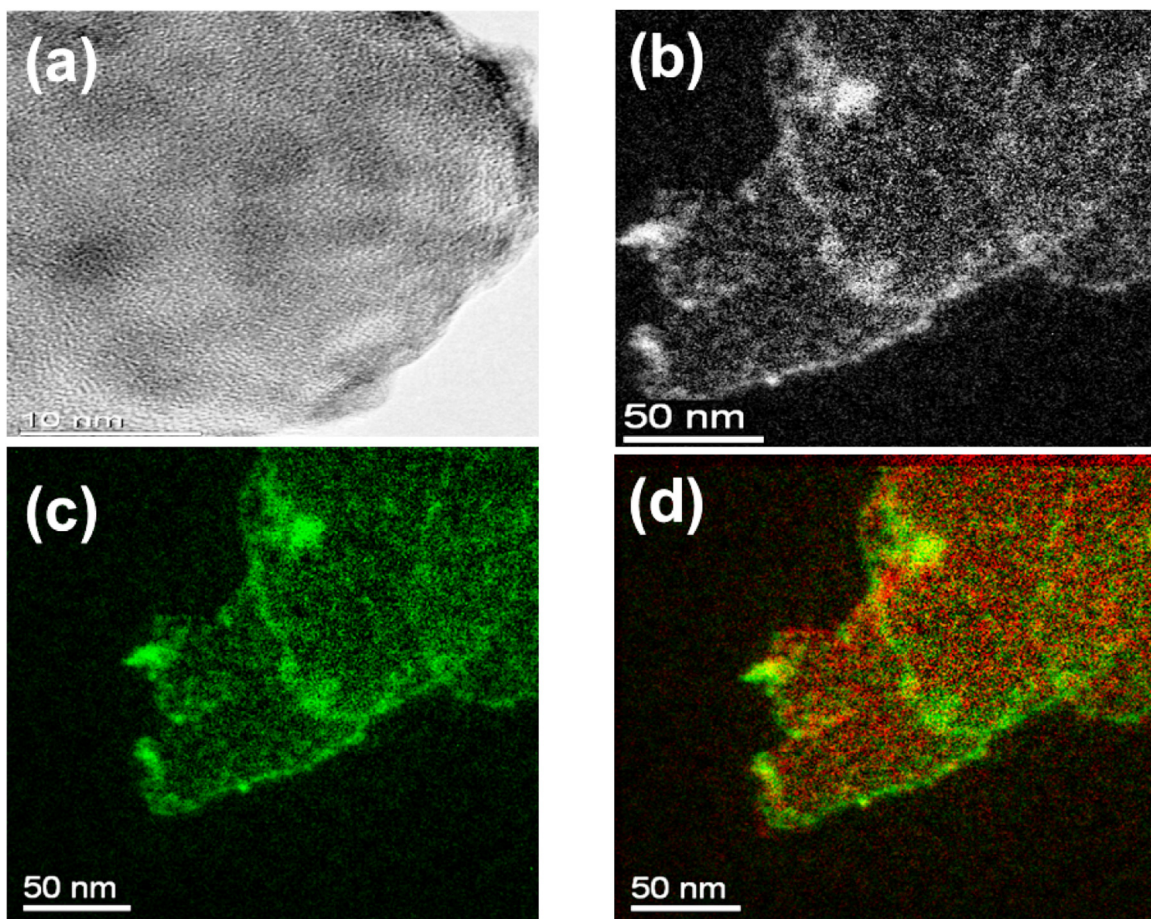


**Fig. 2.** (a), (b) FE-TEM images, and EELS mappings of (c) Ce (green), and (d) Fe (red) and Ce (green) of the CeFe-Z catalyst.

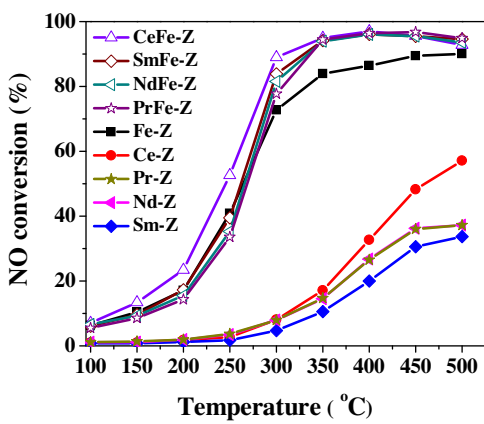


**Fig. 3.** SCR performances of NO conversion with  $\text{NH}_3$  over various mono- and bimetallic catalysts. Reaction conditions:  $[\text{NH}_3] = [\text{NO}] = 500 \text{ ppm}$ ,  $[\text{O}_2] = 2.9\%$ , catalyst mass = 100 mg, total flow rate =  $350 \text{ mL min}^{-1}$ , and GHSV =  $68,000 \text{ cm}^3 \text{ g}^{-1} \text{ h}^{-1}$ .

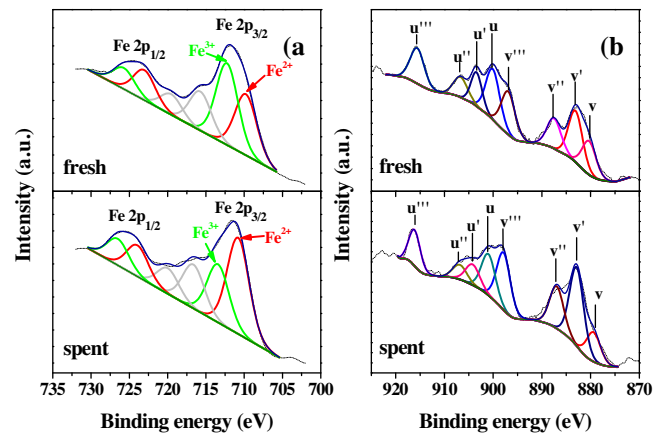


**Fig. 4.** (a) Fe 2p and (b) Ce 3d XPS spectra of the fresh and spent CeFe-Z catalysts (see text). The grey deconvoluted curves in (a) represent satellite peaks.

tified by FE-TEM and metal mappings by EELS technique, as shown in Figs. 1 and 2. After the reduction treatment, typical mono-metal incorporated catalyst such as Fe-Z revealed a well-dispersed metal nanoparticles (NPs; average size *ca.* 3–6 nm) on the surfaces of the H-ZSM-5 zeolite support (Fig. 1a and b), as revealed by the histogram of the particle size distribution (Fig. 1c). Upon incorporating the secondary metal (e.g.,  $M_2 = \text{Ce}$ ), the FE-TEM images (Fig. 2a and b) as well as the EELS mapping (Fig. 2c and d) observed for the CeFe-Z catalyst show uniform and overlapping Ce and Fe distribution with respective average nanoparticle size of *ca.* 2–5 nm (Fig. S6; SI†), indicating a homogenous coverage of both metals.

### 3.2. Catalytic performance

The catalytic performances of mono- and bimetallic catalysts during SCR of NO with  $\text{NH}_3$  are depicted in Fig. 3. For the  $M_1\text{-Z}$  ( $M_1 = \text{Fe, Ce, Pr, Nd, and Sm}$ ) catalysts, it is found that the Fe-Z exhibited a much better catalytic activity of NO conversion (>80%) at the temperature range of 350–500 °C compared to the other catalysts (typically <50%). On the other hand, zeolite supported bimetallic  $M_2\text{Fe-Z}$  ( $M_2 = \text{Ce, Pr, Nd, and Sm}$ ) catalysts exhibited even higher activities than the  $M_1\text{-Z}$  ones, indicating that the incorporation of a secondary Lanthanide metal indeed provokes enhancement in NO conversion. In general, the bimetallic supported catalysts showed excellent SCR activities (>90%) within the temperature of 350–500 °C. Among them, the CeFe-Z catalyst obviously exhibits the best SCR performance with NO conversion exceeding 95%. Moreover, the overall performance somewhat extended to a broader temperature range and shifted toward lower temperatures. Thus, it is conclusive that the incorporation of Ce onto the Fe-ZSM-5 catalyst tends to further enhance the overall catalytic activity at lower reaction temperatures, which is one of the criterion for the SCR performance. It is noteworthy that the structural frameworks of the supported metal catalysts prepared by means of the reflux method remained practically unchanged even after the SCR reaction, as illustrated for by the  $^{27}\text{Al}$  MAS NMR spectra of the Fe-Z and the CeFe-Z catalysts (Fig. S7; SI†). This confirms the absence of a dealumination effect in these supported catalysts with well-dispersed metal NPs during the SCR reaction. Since optimal catalytic performances were observed for the Fe-Z and the CeFe-Z catalysts, discussions hereafter will be focused mostly on these two representative mono- and bimetallic catalysts.

### 3.3. Surface property

To gain further insight on the surface properties of the mono- ( $M_1\text{-Z}$ ) and bimetallic ( $M_2\text{Fe-Z}$ ) catalysts, XPS spectra of the two representative catalysts (*viz.* Fe-Z and CeFe-Z) before and after the SCR reaction were examined over the spectral regions of Fe 2p and Ce 3d. The Fe 2p XPS spectrum of the fresh Fe-Z catalysts exhibited two primary bands centering at *ca.* 723.2 and 710.2 eV due to  $\text{Fe 2p}_{1/2}$  and  $2p_{3/2}$  levels, respectively (Fig. S8a; SI†), revealing the possible presences of  $\alpha\text{-Fe}_2\text{O}_3$  ( $\text{Fe}^{3+}$  ions) and  $\text{FeO}$  ( $\text{Fe}^{2+}$  ion) species [30,45–47]. In this context, a complete reduction of  $\text{Fe}^{3+}$  to  $\text{Fe}^0$  seems unlikely, because if it did occur, a peak with the binding energy of *ca.* 706.7 eV would be anticipated [48]. After the SCR reaction, two similar bands with binding energies of *ca.* 723.5 and 710.4 eV were observed for the spent Fe-Z catalyst (Fig. S8b; SI†). A closer examination of the deconvoluted Fe 2p spectra of the fresh and spent Fe-Z catalysts revealed the presences of some satellite peaks in addition to the main peaks accountable for the  $\text{Fe}^{2+}$  and  $\text{Fe}^{3+}$  species [48,49], as shown in Fig. S8 (SI†). Accordingly, further quantitative analyses based on the primary  $\text{Fe 2p}_{3/2}$  band showed that a relative  $\text{Fe}^{3+}/\text{Fe}^{2+}$  ratio of 1.79 and 0.60 may be inferred for the fresh and spent Fe-Z, respectively. Likewise, the Fe 2p XPS spectra of the CeFe-Z catalyst obtained before and after the SCR reaction also show doublet main peaks at (723.3, 710.1) and (724.3, 711.2) eV anticipated for the  $\text{Fe 2p}_{1/2}$  and  $2p_{3/2}$  levels, respectively (Fig. 4a). Consequently, a relative  $\text{Fe}^{3+}/\text{Fe}^{2+}$  ratio of 1.34 and 0.60 was observed for the fresh and spent CeFe-Z, respectively. Compared to the fresh Fe-Z and CeFe-Z catalysts, notable decrease in  $\text{Fe}^{3+}/\text{Fe}^{2+}$  ratio was observed for their respective spent counterpart, indicating that  $\text{Fe}^{2+}$  species were indeed the primary active sites for  $\text{NH}_3\text{-SCR}$  of NO [50–53], during which considerable amounts of ferric ions were reduced to  $\text{Fe}^{2+}$ . It is noteworthy that more amount of  $\text{Fe}^{2+}$  was also found in CeFe-Z than the monometallic Fe-Z sample. This may be ascribed due to redox process of  $\text{Ce}^{4+}/\text{Ce}^{3+}$ , which provoke transfer of electrons to  $\text{Fe}^{3+}$  [11].

The Ce 3d XPS spectra of the CeFe-Z catalyst show bands with multiple shake-up and shake-down satellites (Fig. 4b); the bands with binding energy around 875–895 and 895–910 eV may be ascribed due to the  $\text{Ce 3d}_{5/2}$  and  $\text{Ce 3d}_{3/2}$  levels, respectively [54]. These spectra may be deconvoluted into eight components, where  $\text{v}'$ s and  $\text{u}'$ s represent the bands accountable for the  $\text{Ce 3d}_{5/2}$  and  $\text{Ce 3d}_{3/2}$  level, respectively, and the presences of  $\text{Ce}^{3+}$  ( $\text{v}'$  and  $\text{u}'$  only) and  $\text{Ce}^{4+}$  species. Among them, the singlet  $\text{u}''$  band is normally used as an indicator for quantitative measurements of the relative  $\text{Ce}^{4+}$  concentration in the substrate [55]. Accordingly, out of the total  $\text{Ce}^{3+}$  and  $\text{Ce}^{4+}$  species, a relative  $\text{Ce}^{4+}$  amount of 12.1 and 9.3% was

determined for the fresh and spent CeFe-Z catalyst, respectively. Thus, it is indicative that, over the bimetallic CeFe-Z catalyst, the presence of  $\text{NO}_x$  during SCR tends to provoke a substantial reduction of  $\text{Ce}^{4+}$  to  $\text{Ce}^{3+}$  species.

Additional chemisorption study by temperature-programmed reduction of hydrogen ( $\text{H}_2\text{-TPR}$ ) revealed that the Ce-Z catalyst showed  $\text{H}_2$  consumption peaks at *ca.* 400, 580 and 680 °C (Fig. S9; SI†), which may be attributed to surface/shell reduction of  $\text{CeO}_2$ , reduction of surface capping oxygen, and reduction of surface  $\text{Ce}^{4+}$  to  $\text{Ce}^{3+}$ , respectively [56–58]. Whereas, the Fe-Z catalyst exhibited overlapping peaks at three distinct regions. The  $\text{H}_2$  consumption peak occurring at 380–400 °C corresponds to reduction of  $\text{Fe}^{3+}$  (from bare  $\text{Fe}^{3+}$  ions, oxo-Fe, or species such as  $\text{FeO}^+$ ,  $\text{Fe(OH)}^{2+}$  or  $[(\text{OH})\text{FeOFe(OH)}]^{2+}$ ) to  $\text{Fe}^{2+}$  [30]. The reduction peak at *ca.* 500 and 580 °C may be assigned due to reduction of  $\text{Fe}_3\text{O}_4$  nanoclusters to  $\text{FeO}$  and reduction of  $\text{FeO}$  to  $\text{Fe}^0$ , respectively. Species such as  $\alpha\text{-Fe}_2\text{O}_3$  nanoclusters has been identified to be reduced at *ca.* 350 °C [59]. On the other hand, the bimetallic CeFe-Z catalyst revealed three major  $\text{H}_2$  consumption peaks at 380, 400–500, and 500–620 °C. The broader reduction peak observed for the CeFe-Z at higher temperatures compared to that in the Fe-Z may be ascribed to the simultaneous reduction of both Fe and Ce species. The overlapping  $\text{H}_2$  reduction peaks observed for the CeFe-Z thus indicates a strong interaction between the two metal species. It is anticipated that such synergistic interactions between Fe and Ce species should be responsible for the enhanced SCR activity observed for the bimetallic catalyst.

### 3.4. Acidic property

#### 3.4.1. $\text{NH}_3\text{-TPD}$

Ammonia-TPD is a conventional technique commonly used for acidity characterization of solid catalysts, although its capability in probing detailed distribution of Brønsted acidic sites in solid acid catalysts remains a debatable issue [31–34,60,61]. The  $\text{NH}_3\text{-TPD}$  profiles of the pristine H-ZSM-5, and mono- ( $M_1\text{-Z}$ ;  $M_1 = \text{Fe, Ce, Pr, Nd, Sm}$ ) and bimetallic ( $M_2\text{Fe-Z}$ ;  $M_2 = \text{Ce, Pr, Nd, Sm}$ ) catalysts are shown in Fig. S10 (SI†). The pristine H-ZSM-5 shows two broad  $\text{NH}_3$  desorption peaks centered at *ca.* 177 and 380 °C. The former peak at lower temperature (typically <200 °C) may be attributed to  $\text{NH}_3$  desorbed from weak silanol ( $\text{Si-OH}$ ) [61–63]. Akah et al. [64] suggested that the presence of weak Lewis acidic sites may also be associated with the low-temperature desorption peak. On the other hand, the desorption peaks occurs at higher temperatures (typically within 350–550 °C) is normally assigned to  $\text{NH}_3$  strongly adsorbed on acidic hydroxyl groups, *i.e.*, Brønsted acidic sites [65].

The concentrations of acidic sites in various mono- ( $M_1\text{-Z}$ ;  $M_1 = \text{Fe, Ce, Pr, Nd, and Sm}$ ) and bimetallic ( $M_2\text{Fe-Z}$ ;  $M_2 = \text{Ce, Pr, Nd, and Sm}$ ) catalysts may be inferred by the amounts of desorbed  $\text{NH}_3$  deduced from the TPD profiles, as depicted in Table 1. Similar to the pristine H-ZSM-5, all mono-metal ( $M_1\text{-Z}$ ) catalysts show two main desorption peaks at *ca.* 177 and 380 °C. However, upon incorporating metal onto zeolite, notable increases in desorption areas of both peaks were found, revealing notable increases in the amount of acidic sites. However, no significant shift in desorption temperature was observed upon metal doping, suggesting that no significant change in the overall acidic strength may be inferred. The high-temperature desorption peak (at 380 °C) observed for the  $M_1\text{-Z}$  catalysts therefore reflect the amount of  $\text{NH}_3$  desorbed from strong metal cationic active sites [66], which obey the following descending order:  $\text{Fe-Z} > \text{Ce-Z} > \text{Pr-Z} \approx \text{Nd-Z} \approx \text{Sm-Z} \gg \text{H-ZSM-5}$  (Fig. S10A; SI†). It is noted that, upon introducing Fe metal onto the H-ZSM-5, the amount of strong acidic sites notably increased from 0.69 to 1.59 mmol g<sup>-1</sup> (Table 1).

As for the bimetallic  $M_2\text{Fe-Z}$  ( $M_2 = \text{Ce, Pr, Nd, and Sm}$ ) catalysts, the corresponding  $\text{NH}_3\text{-TPD}$  profiles exhibited an extra

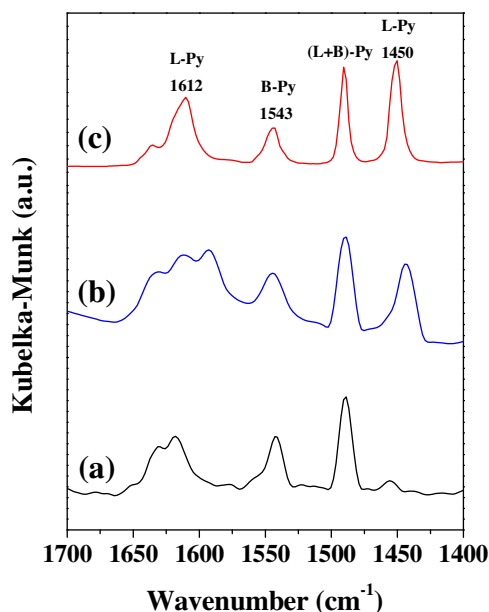


**Fig. 5.** FT-IR spectra of adsorbed pyridine (at 100 °C) in (a) pristine H-ZSM-5, (b) Fe-Z, and (c) CeFe-Z catalysts.

high-temperature weak desorption peak at *ca.* 525 °C (see Fig. S10B; SI†) in addition to afore discussed peaks observed for the  $M_1\text{-Z}$  catalysts. This reflects that the incorporation of the secondary Lanthanide metal ( $M_2$ ) effectively enhance the acidity of the catalyst through a synergistic effect with the primary active Fe species. The appearance of the high temperature desorption peak in these bimetallic  $M_2\text{Fe-Z}$  catalysts may be *a priori* attributed to desorption of  $\text{NH}_3$  from the strong Brønsted and/or Lewis acidic sites (*vide infra*). For the CeFe-Z catalyst, the incorporation of Ce onto the Fe-ZSM-5 was found to improve thermal stability, oxygen uptake capacity, and redox property of the catalyst, which promote releasing/sharing of oxygen in the skeletal framework of zeolite [67], it is speculated that strong interactions between Fe and Ce may provoke formation of Fe active species, leading to the improved catalytic activity observed.

#### 3.4.2. Pyridine-IR

FT-IR of adsorbed pyridine is also a technique commonly used for acidity characterization of solid acid catalysts. One of the major advantages of this method is that it renders simultaneous identification of Brønsted and Lewis acidic sites in the sample [31,68–73]. The IR spectra observed for pyridine adsorbed on zeolites normally exhibit multiple characteristic bands. Typically, the vibrational bands appear at *ca.* 1540–1548 and 1445–1460 cm<sup>-1</sup> are attributed to pyridine adsorbed on acidic  $\text{H}^+$  (*i.e.*, Brønsted acid site; hereafter denoted as B-Py) and Lewis (denoted as L-Py) acidic sites, respectively. In addition, bands responsible for hydrogen-bonded pyridine (hb-Py) normally show up in the range of *ca.* 1440–1447 and 1580–1600 cm<sup>-1</sup>, while physisorbed pyridine (ph-Py) may be identified by bands located at *ca.* 1439 and 1580 cm<sup>-1</sup> [68,69]. As a consequence, a severe overlapping of the vibrational bands prohibits an effective discernment of adsorption sites. However, since the adsorption strength of pyridine at various adsorption sites normally follow the trend: ph-Py < hb-Py < L-Py, B-Py, desorption of pyridine from different sites may be resolved by performing experiments at different temperatures [70]. For example, the influences arising from ph-Py and hb-Py species may be effectively removed when the experiments were carried out at elevated temperatures (typically  $\geq 100$  °C).

**Table 2**

Variations of Brønsted vs Lewis Acidity in the pristine H-ZSM-5 (Si/Al = 15), Fe-Z, and CeFe-Z catalysts before and after the SCR reaction measured by pyridine-IR at different temperatures.

Catalyst	T (°C)	Peak area		B/L
		B-Py (1543 cm <sup>-1</sup> )	L-Py (1445 cm <sup>-1</sup> )	
H-ZSM-5	100	2.50	1.34	1.87
	200	2.30	0.92	2.50
	300	1.94	0.64	3.03
	400	1.06	0.34	3.12
Fe-Z (fresh)	100	2.17	4.23	0.51
	200	1.64	1.30	1.26
	300	1.52	1.06	1.43
	400	0.89	0.53	1.68
Fe-Z (spent)	100	2.51	3.44	0.73
	200	1.88	1.55	1.21
	300	1.21	0.89	1.36
	400	0.28	0.25	1.12
CeFe-Z (fresh)	100	1.97	4.52	0.44
	200	1.32	2.52	0.52
	300	0.70	0.88	0.80
	400	0.28	0.25	1.12
CeFe-Z (spent)	100	2.24	4.74	0.47
	200	1.97	2.37	0.83
	300	0.32	1.60	0.83

Fig. 5 shows the typical pyridine-IR spectra of the pristine H-ZSM-5, Fe-Z, and CeFe-Z catalysts measured at 100 °C. The band appears at ca. 1543 cm<sup>-1</sup> should arise from pyridine adsorbed on Brønsted acidic sites (B-Py), while bands at ca. 1445–1460 and 1612 cm<sup>-1</sup> may be attributed to pyridine adsorbed on Lewis acidic sites (L-Py). Moreover, the band at ca. 1490 and 1590 cm<sup>-1</sup> may be ascribed due to collective contributions of L-Py and B-Py and hydrogen-bonded pyridine (hb-Py), respectively [68,69]. As such, the areas of the bands at ca. 1543 and 1445 cm<sup>-1</sup> are commonly used to evaluate the concentrations of Brønsted and Lewis acidic sites [68,69]. As expected, the pyridine-IR spectrum of the pristine H-ZSM-5 shows predominantly adsorption band of B-Py, although some Lewis acidity are also visible likely due to the presence of Al<sup>3+</sup> species. As shown in Table 2 (see also Fig. S11a; SI†), the relative area of the B-Py vs L-Py increase with increasing temperature of adsorption, indicating a stronger adsorption strength of pyridine with Brønsted than Lewis acidic sites. It is noted that upon incorporating metal onto the H-ZSM-5 zeolite, a notable increase in Lewis acidity was evident. On the basis of the peak area ratio of the B-Py and the L-Py bands at 1543 and 1445 cm<sup>-1</sup> measured at 100 °C, respectively, notable differences in the relative concentration of the Brønsted vs Lewis acidic sites (*i.e.*, B/L ratio) are also evident. Upon introducing Fe and CeFe metal onto the MFI zeolite, the B/L ratio decreased from ca. 1.87 of the pristine H-ZSM-5 to 0.51 and 0.44 for that of the fresh Fe-Z and the CeFe-Z, respectively (Table 2). Clearly, the incorporation of Fe and secondary Lanthanide-metal (*e.g.*, Ce) promote formation of Lewis acidity in the supported zeolite catalysts.

To access variations of Brønsted and Lewis acidity of the supported mono- and bimetallic catalysts, pyridine-IR spectra of Fe-Z and CeFe-Z samples were also recorded before and after SCR reaction, as shown in Fig. S11 (SI†) and Fig. 6, respectively. The relevant variations of Brønsted vs Lewis acidic sites (B/L ratio) of assorted catalysts are also depicted in Table 2. Similar to the pristine H-ZSM-5, a consistent increase in Brønsted acidity (or increase in B/L ratio) with increasing temperature of pyridine adsorption may be inferred for the fresh Fe-Z and CeFe-Z catalysts. It is noted that substantial amount of Brønsted acidities are evident in these mono- and bimetal promoted MFI catalysts even at desorption temperature as high as 400 °C, suggesting the presences of acidic sites with strong acidic strengths. The results are in line with the high temperature NH<sub>3</sub> desorption peak observed for the bimetallic M<sub>2</sub>Fe-Z catalysts (Fig. S10B; SI†). Moreover, the B/L ratio derived from the

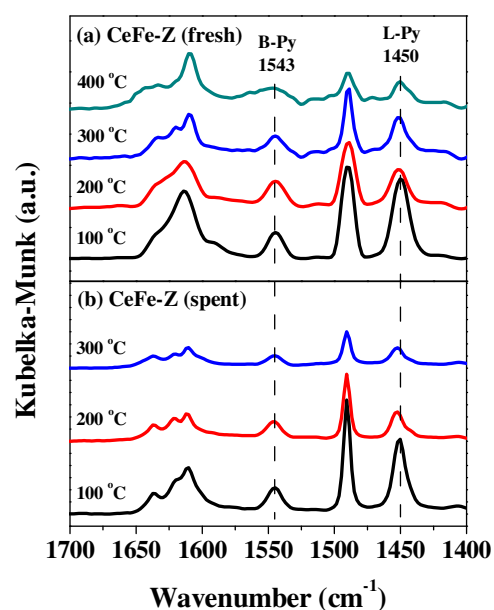


Fig. 6. FT-IR spectra of adsorbed pyridine measured at different temperatures on the CeFe-Z catalyst (a) before and (b) after the SCR reaction.

spent Fe-Z and CeFe-Z catalysts after the SCR reaction is also found to increase with increasing temperature of pyridine desorption. It is noted that the B/L ratio derived from spent catalysts are slightly larger than those derived from the fresh catalysts. This indicates that some of the strong Lewis acidic sites may be inhibited or deactivated during SCR of NO with NH<sub>3</sub>, in excellent agreement with the <sup>31</sup>P NMR data (*vide infra*).

#### 3.4.3. <sup>31</sup>P MAS NMR of adsorbed TMPO

As elaborated in several reviews on acidity characterization of solid acids [34,35], solid-state <sup>31</sup>P MAS NMR of adsorbed trialkylphosphine oxides (R<sub>3</sub>PO) is a unique technique for probing the detailed features, *viz.* types (Brønsted and/or Lewis acid), strength, concentration (mount), and location (intra- vs extra-crystalline), of acidic sites in various solid acid catalysts. Taking the trimethylphosphine oxide (TMPO; whose kinetic diameter is comparable to the typical pore size of 10-membered rings zeolites, such as ZSM-5) molecule as an example, the linear correlation between the observed <sup>31</sup>P NMR chemical shift of TMPO (or its R<sub>3</sub>PO analogous) and proton affinity (or deprotonation energy) [34–36] facilitates a convenient scale for acidic strength. In other words, the higher the observed <sup>31</sup>P NMR chemical shift ( $\delta^{31}\text{P}$ ) of TMPO, the higher the acidic strength of the corresponding acid sites. Moreover, such <sup>31</sup>P R<sub>3</sub>PO NMR approach also renders quantitative characterization of acidic sites when performing the experiments in conjunction with elemental analysis [33–35], making possible to determine distribution and concentration of acidic sites. Moreover, the same <sup>31</sup>P R<sub>3</sub>PO NMR approach may be exploited for discernment of acidic sites located in intra-crystalline pores vs extra-crystalline surfaces of the porous solid acid catalysts by using probe molecules with varied sizes [33–35]. Our previously study on a series of metal-promoted sulfated zirconia catalysts [60] have demonstrated that acidity characterization exploiting the <sup>31</sup>P TMPO NMR approach affords more reliable information regarding to detailed features of the acidic sites. Accordingly, more accurate information on the type, strength, and distribution of acidic sites may be inferred compared to the conventional techniques such as NH<sub>3</sub>-TPD and pyridine-IR (*vide supra*).

Figs. 7 and 8 show the <sup>31</sup>P MAS NMR spectra of TMPO adsorbed on the pristine H-ZSM-5, Fe-Z and CeFe-Z catalysts before and

**Table 3**

$^{31}\text{P}$  NMR chemical shift assignments and relative concentrations of acidic sites of the pristine H-ZSM-5 (Si/Al = 15), Fe-Z, and CeFe-Z catalysts before and after the SCR reaction measured by  $^{31}\text{P}$  MAS NMR of adsorbed TMPO probe molecule<sup>a</sup>.

Chemical shift (ppm)	100–101	90–93	83–85	73–76	64–68	60–63	53–55	41–45	<40	B/L ratio
Acid type	L	L	B(+L)	B(+L)	B(+L)	B(+L)	B(+L)	P	P	
Catalyst	Acid concentration (%)									
H-ZSM-5 (dehydrated)	—	—	4.9	16.6	43.1(B)	15.2	20.2	P	P	4.35
H-ZSM-5 (hydrated)	—	—	1.1	14.5	61.8	5.8	16.8	—	—	ND
Fe-Z (fresh)	12.1	2.1	4.6(L)	4.6(B)	66.6	—	10.0(B)	P	—	0.77
Fe-Z (hydrated)	—	—	—	16.1	28.9	37.9	17.1	P	P	ND
Fe-Z (spent)	16.4	—	4.5	3.5	71.3	—	4.3	P	—	0.93
CeFe-Z (fresh)	10.4	7.7	—	22.8(B)	49.2	----	9.9(B)	P	P	1.42
CeFe-Z (hydrated)	—	—	—	32.9	26.0	23.2	17.9	P	P	ND
CeFe-Z (spent)	7.8	5.9	—	23.1	43.7	—	19.5	P	P	1.92

<sup>a</sup> Notations: L = Lewis acid; B = Brønsted acid; B(+L) = possibly involves both Brønsted and Lewis acidity; P = physisorbed TMPO; √ = present; B/L = relative ratio of Brønsted vs Lewis acidity; ND = not determined. Note that since the observed  $\delta^{31}\text{P}$  in such solid-state NMR measurements has an experimental error of ca.  $\pm 2\text{--}3$  ppm due to dipolar broadening, overlapping resonance peaks within the error range were combined during analyses of peak areas (*i.e.*, acid concentration) to avoid complication.

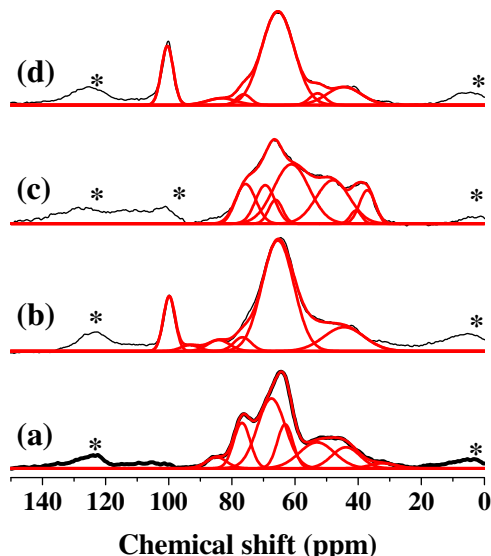


**Fig. 7.**  $^{31}\text{P}$  MAS NMR spectra of TMPO adsorbed on various catalysts: (a) pristine H-ZSM-5, (b) fresh Fe-Z, (c) hydrated fresh Fe-Z, and (d) spent Fe-Z after the SCR reaction. The curves in red represent results from Gaussian spectral deconvolution and the asterisks denote spinning sidebands. (For interpretation of the references to colour in this figure legend, the reader is referred to the web version of this article.)

after the SCR reaction. On the basis of spectral analyses by Gaussian deconvolution,  $^{31}\text{P}$  MAS NMR spectrum observed for the pristine H-ZSM-5 support exhibited the anticipated multiple  $^{31}\text{P}$  resonance signals at 85, 77, 67, 63, 53, 44, and 32 ppm, in accordance with those reported previously [33]. The peaks with  $\delta^{31}\text{P}$  below 45 ppm may be unambiguously attributed to physisorbed and mobile TMPO, whereas the resonances with  $\delta^{31}\text{P}$  above 53 ppm may be attributed to TMPO adsorbed at various Brønsted acidic sites, forming the TMPOH<sup>+</sup> ionic complexes with varied acidic strengths [33–35]. Moreover, it has been shown that  $^{31}\text{P}$  resonances with  $\delta^{31}\text{P}$  higher than 86 ppm may be considered as TMPO adsorbed on ultra-strong acidic sites with acidic strength beyond superacidity [34–37]. It is indicative that while the pristine H-ZSM-5 possesses predominantly Brønsted acidic sites with moderate acidic strengths ( $\delta^{31}\text{P}$ –65 ppm), incorporation of Fe and secondary Lanthanide metal onto the H-ZSM-5 provoke formation of strong Lewis acidic sites (Figs. 7 and 8). In view of the strong proton affinity nature of Lewis acidic sites in solid acids, vanishing of Lewis acidity is anticipated when the catalyst is exposed to water, if they are indeed present in the catalyst [33–35]. As such, to verify the existence of Lewis acidity, additional experiments conducted on fully hydrated Fe-Z and CeFe-Z catalyst samples were also performed, as

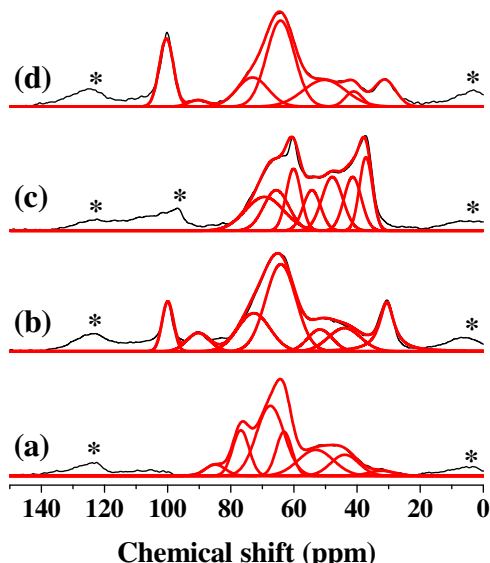


**Fig. 8.**  $^{31}\text{P}$  MAS NMR spectra of TMPO adsorbed on various catalysts: (a) pristine H-ZSM-5, (b) fresh CeFe-Z, (c) hydrated fresh CeFe-Z, and (d) spent CeFe-Z after the SCR reaction. The curves in red represent results from Gaussian spectral deconvolution and the asterisks denote spinning sidebands. (For interpretation of the references to colour in this figure legend, the reader is referred to the web version of this article.)

shown in Figs. 7 c and 8 c. The detailed  $\delta^{31}\text{P}$  assignments and relative concentrations of acidic sites of the pristine H-ZSM-5, Fe-Z, and CeFe-Z catalysts before and after SCR reaction are depicted in Table 3.

Upon incorporating Fe onto the MFI zeolite,  $^{31}\text{P}$  resonances of adsorbed TMPO at 101, 93, 84, 77, 66, and 54 ppm were observed (Fig. 7b and Table 3). By comparing with the peak areas observed for the pristine H-ZSM-5, the incorporation of Fe metal clearly induced formation of very strong Lewis acidic sites with  $\delta^{31}\text{P}$  at *ca.* 101 and 93 ppm at the expanses of mostly Brønsted acidic sites having relatively lower acidic strengths (cf.  $\delta^{31}\text{P}$  observed for the dehydrated H-ZSM-5 at *ca.* 77, 63, and 53 ppm). A closer examination of the  $^{31}\text{P}$  NMR spectra observed for the fully hydrated Fe-Z catalyst reveals that resonances with  $\delta^{31}\text{P}$  at *ca.* 66 ppm may be associated with both Brønsted and Lewis acidic sites having somewhat moderate acidic strengths (Fig. 7c). Assuming that all Lewis acid sites were completely transformed into Brønsted acidity in the fully hydrated Fe-Z sample, the relative amount of the total Brønsted (B) vs Lewis (L) acidity in the dehydrated Fe-Z catalyst can therefore be deduced. As can be seen in Table 3, a drastic decrease in B/L ratio was observed for the Fe-Z catalyst (0.77) compared to that of the pristine H-

ZSM-5 (4.35), revealing a substantial increase in Lewis acidity upon incorporating Fe onto the MFI zeolite.

Likewise, for the bimetallic CeFe-Z catalyst, the incorporation of Fe and Ce metals onto the zeolite support also induced formations of very strong Lewis acidic sites with  $\delta^{31}\text{P}$  at ca. 100 and 90 ppm at the expanses of mostly Brønsted acidic sites with relatively weaker acidic strengths (cf.  $\delta^{31}\text{P}$  observed for the pristine H-ZSM-5 at ca. 85, 77, 63, and 53 ppm), as shown in Fig. 8b and Table 3. Further experiments carried out with the fully hydrated CeFe-Z sample verified that the resonances corresponding to  $\delta^{31}\text{P}$  at ca. 100 and 90 ppm may be unambiguously

attributed to the presence of very strong Lewis acidic sites, while the peak at 74 ppm may be associated with both Brønsted and Lewis acidic sites (Fig. 8c). As shown in Table 3, the incorporation of the Ce metal onto the Fe-based MFI zeolites promote formation of ultra-strong Lewis acidity at the expanse of Brønsted acidic sites with moderate or weak acidic strengths. This may readily be seen from the relative distributions of Brønsted vs Lewis acidity for the pristine H-ZSM-5, Fe-Z, and CeFe-Z illustrated in Fig. S12 (SI†). Thus, the higher B/L ratio deduced for the dehydrated CeFe-Z (1.42) than its mono-metal counterpart Fe-Z (0.77), indicating that incorporation of the secondary Lanthanide metal indeed provokes formation of more Brønsted acidity with moderate acidic strength as well as ultra-strong Lewis acidity.

$^{31}\text{P}$  MAS NMR spectra of TMPO adsorbed on the spent Fe-Z and CeFe-Z catalysts after SCR of NO with  $\text{NH}_3$  were also investigated; the results are displayed in Figs. 7 d and 8 d. The corresponding  $\delta^{31}\text{P}$  assignments as well as the types and relative concentrations of acidic sites are also depicted in Table 3. Compared to the fresh Fe-Z catalyst, the strong Lewis acidity corresponding to  $\delta^{31}\text{P}$  at ca. 90 ppm vanished along with the weak Brønsted acidic sites ( $\delta^{31}\text{P}$  at ca. 53 ppm), leading to increases in concentrations of Lewis acidic sites at ca. 101 and 66 ppm, hence, a slight increase in the overall B/L value (from 0.77 to 0.93). On the other hand, while notable decreases in Lewis acidity at ca. 100 and 90 ppm were found for the spent CeFe-Z catalyst, simultaneous increases in Brønsted acidity corresponding to  $\delta^{31}\text{P}$  at ca. 74 and 54 ppm were also observed, leading to an increase in B/L ratio. Thus, the higher B/L ratio observed for the spent CeFe-Z (1.92; see Table 3) compared to its pristine fresh counterpart (1.42), readily indicates the diminishing of ultra-strong Lewis acidity ( $\delta^{31}\text{P} \geq 86$  ppm) at the expanse of formation of moderate Brønsted acidity at  $\delta^{31}\text{P}$  ca. 53–55 ppm (Table 3). It is noteworthy that an increase in Brønsted acidity of the catalyst would render more adsorption of  $\text{NH}_3$ , leading to an enhanced NO conversion. The higher B/L ratio observed for the fresh CeFe-Z (1.42) compared to the Fe-Z (0.77) is also favorable for a stronger reduction of NO by  $\text{NH}_3$ , hence, facilitating the  $\text{NH}_3$  activation process. Clearly, these results obtained from the  $^{31}\text{P}$  TMPO NMR approach are much more reliable than those derived from pyridine-IR studies (see Table 2), whose B/L ratios were deduced based on only peak areas of specific bands corresponding to Brønsted and Lewis acid sites rather than their overall contributions.

Thus, it is conclusive that the incorporations of the primary Fe metal and a secondary Lanthanide metal (Ce) promote formation of very strong Lewis acidic sites with  $\delta^{31}\text{P}$  exceeding the threshold for superacidity (86 ppm) [34–37]. For the bimetallic supported CeFe-Z sample, which exhibited the best catalytic activity during the SCR reaction, notable increases in Brønsted acid sites with moderate acidic strengths were also observed. It is indicative that a synergistic effect of such Brønsted acidity of the zeolite support together with the strong Lewis acidity arising from the concurrent presence of the active  $\text{Fe}^{2+}$  and  $\text{Ce}^{3+}$  (possibly also  $\text{Ce}^{4+}$ ) metal ion species resulted in an effective lowering of energy barrier, thus, the superior SCR activity observed for the CeFe-Z catalyst. These findings are in line with existing reports, which proposed that the presence of

Ce not only promote stability of the Fe-ZSM-5 [5] but also enhances the oxidation of  $\text{NH}_3$  during the SCR reaction [27].

#### 4. Conclusions

An alternate approach, namely solid-state  $^{31}\text{P}$  TMPO MAS NMR, has been exploited to investigate the role of acidity on catalytic performances of various mono- ( $M_1\text{-ZSM-5}$ ;  $M_1 = \text{Fe}, \text{Ce}, \text{Pr}, \text{Nd}$ , and Sm) and bimetallic ( $M_2\text{Fe-ZSM-5}$ ;  $M_2 = \text{Ce}, \text{Pr}, \text{Nd}$ , and Sm) catalyst supported on H-ZSM-5 ( $\text{Si}/\text{Al} = 15$ ) zeolite during SCR of NO by  $\text{NH}_3$ . Accordingly, the variations in Brønsted and Lewis acidities may be probed simultaneously, and the results were compared with that obtained by conventional acidity characterization techniques, such as  $\text{NH}_3$ -TPD and pyridine-IR. Compared to the Fe-ZSM-5 catalyst, the superior SCR activity observed for the bimetallic CeFe-ZSM-5 catalyst may be attributed to the formation of strong Lewis acid sites upon incorporating the secondary metal (Ce) to the Fe-based MFI zeolites. Along with the surface information obtained by XPS study, it is conclusive that the incorporation of Fe and Ce metals leads to formation of various Fe ( $\text{Fe}^{2+}$  and  $\text{Fe}^{3+}$ ) and Ce ( $\text{Ce}^{3+}$  and  $\text{Ce}^{4+}$ ) ion species, which in turn promotes formations of strong Lewis acidic sites and notable increases in Brønsted acid sites with moderate acidic strengths. As a result, a collective effect of the Brønsted acidity originated from the MFI zeolite support and the strong Lewis acidity induced by the incorporated metal species is responsible for the superior catalytic activity observed for the CeFe-ZSM-5 during the  $\text{NH}_3$ -SCR reaction. This work also demonstrates that acidity characterization exploiting the  $^{31}\text{P}$  TMPO NMR approach is unique in providing detailed acidic features of sophisticated solid acids, such as the multifunctional metal supported zeolite catalysts studied herein.

#### Acknowledgments

The supports of this work by the Ministry of Science and Technology, Taiwan (NSC 101-2113-M-001-020-MY3 and MOST 104-2113-M-001-019 to SBL and Natural Science Foundation of Zhejiang province, China (No. LY13B070005 to XH) are gratefully acknowledged. SHB thanks the Nano Science and Technology Program, Taiwan International Graduate Program (TIGP), Academia Sinica for the scholarship. XH is grateful to the visiting research fellowships from the Institute of Atomic and Molecular Sciences, Academia Sinica.

#### Appendix A. Supplementary data

Supplementary data associated with this article can be found, in the online version, at <http://dx.doi.org/10.1016/j.molcata.2016.07.036>.

#### References

- [1] H. Bosch, F. Janssen, *Catal. Today* 2 (1988) 369–379.
- [2] B. Li, Z. Huang, X. Huang, S. Kou, F. Liu, X. Zhang, H. Yang, *RSC Adv.* 6 (2016) 6300–6307.
- [3] L. Olsson, H. Sjövall, R.J. Blint, *Appl. Catal. B* 81 (2008) 203–217.
- [4] X. Wang, S. Yu, H. Yang, S. Zhang, *Appl. Catal. B* 71 (2007) 246–253.
- [5] R.Q. Long, R.T. Yang, *J. Am. Chem. Soc.* 121 (1999) 5595–5596.
- [6] A.Z. Ma, W. Grünert, *Chem. Commun.* (1999) 71–72.
- [7] H.Y. Chen, W.M.H. Sachtleber, *Catal. Today* 42 (1998) 73–83.
- [8] L. Zhu, L. Zhang, H. Qu, Q. Zhong, *J. Mol. Catal. A* 409 (2015) 207–215.
- [9] T. Du, H. Qu, Q. Liu, Q. Zhong, W. Ma, *Chem. Eng. J.* 262 (2015) 1199–1207.
- [10] I. Malpartida, O. Marie, P. Bazin, M. Daturi, X. Jeandel, *Appl. Catal. B* 113–114 (2012) 52–60.
- [11] Z. Liu, Y. Liu, B. Chen, T. Zhu, L. Ma, *Catal. Sci. Technol.* (2016), <http://dx.doi.org/10.1039/C5CY02278A>.
- [12] S. Brandenberger, O. Kröcher, A. Wokaun, A. Tissler, R. Althoff, *J. Catal.* 268 (2009) 297–306.
- [13] M. Schwidder, M.S. Kumar, U. Bentrup, J. Pérez-Ramírez, A. Brückner, W. Grünert, *Microporous Mesoporous Mater.* 111 (2008) 124–133.

- [14] P. Boroń, L. Chmielarz, J. Gurgul, K. Łątka, B. Gil, J.M. Krafft, S. Dzwigaj, *Catal. Today* 235 (2014) 210–225.
- [15] K. Rahkamaa-Tolonen, T. Maunula, M. Lomma, M. Huuhtanen, R.L. Keiski, *Catal. Today* 100 (2005) 217–222.
- [16] H.Y. Huang, R.Q. Long, R.T. Yang, *Appl. Catal. A* 235 (2002) 241–251.
- [17] H. Sjövall, L. Olsson, E. Fridell, R.J. Blint, *Appl. Catal. B* 64 (2006) 180–188.
- [18] A.L. Kustov, T.W. Hansen, M. Kustova, C.H. Christensen, *Appl. Catal. B* 76 (2007) 311–319.
- [19] R.Q. Long, R.T. Yang, *J. Catal.* 198 (2001) 20–28.
- [20] R.Q. Long, R.T. Yang, *J. Catal.* 207 (2002) 224–231.
- [21] M.J. Li, Y.H. Yeom, E. Weitz, W.M.H. Sachtleber, *Catal. Lett.* 112 (2006) 129–132.
- [22] S. Brandenberger, O. Kröcher, A. Tissler, R. Althoff, *Catal. Rev. Sci. Eng.* 50 (2008) 492–531.
- [23] J. Eng, C.H. Bartholomew, *J. Catal.* 171 (1997) 27–44.
- [24] D.A. Peña, B.S. Uphade, P.G. Smirniotis, *J. Catal.* 221 (2004) 421–431.
- [25] X. Liang, J. Li, Q. Lin, K. Sun, *Catal. Commun.* 8 (2007) 1901–1904.
- [26] C.T. Hung, K.C. Lin, C.B. Wang, S.H. Begum, X. Han, S.B. Liu, *Adv. Porous Mater.* (2016), <http://dx.doi.org/10.1166/apm.2016.1117>.
- [27] G. Zhou, B. Zhong, W. Wang, X. Guan, B. Huang, D. Ye, H. Wu, *Catal. Today* 175 (2011) 157–163.
- [28] M. Stanculescu, P. Bulsink, G. Caravaggio, L. Nossova, R. Burich, *Appl. Surf. Sci.* 300 (2014) 201–207.
- [29] Y. Li, H. Cheng, D. Li, Y. Qin, Y. Xie, S. Wang, *Chem. Commun.* (2008) 1470–1472.
- [30] M. Iwasaki, K. Yamazaki, K. Banno, H. Shinjoh, *J. Catal.* 260 (2008) 205–216.
- [31] G. Carja, G. Delahay, C. Signorile, B. Coq, *Chem. Commun.* (2004) 1404–1405.
- [32] J. Pérez-Ramírez, J.C. Groen, A. Brückner, M.S. Kumar, U. Bentrup, M.N. Debbagh, L.A. Villaescusa, *J. Catal.* 232 (2005) 318–334.
- [33] Q. Zhao, W.H. Chen, S.J. Huang, Y.C. Wu, H.K. Lee, S.B. Liu, *J. Phys. Chem. B* 106 (2002) 4462–4469.
- [34] A. Zheng, S.J. Huang, S.B. Liu, F. Deng, *Phys. Chem. Chem. Phys.* 13 (2011) 14889–14901.
- [35] A. Zheng, S. Li, S.B. Liu, F. Deng, *Acc. Chem. Res.* 49 (2016) 655–663.
- [36] A. Zheng, H. Zhang, X. Lu, S.B. Liu, F. Deng, *J. Phys. Chem. B* 112 (2008) 4496–4505.
- [37] A. Zheng, S.J. Huang, W.H. Chen, P.H. Wu, H. Zhang, H.K. Lee, L.C. de Ménorval, F. Deng, S.B. Liu, *J. Phys. Chem. A* 112 (2008) 7349–7356.
- [38] G. Engelhardt, D. Michel, *High Resolution Solid-State NMR of Silicate and Zeolites*, Wiley, New York, 1987.
- [39] J.A. van Bokhoven, D.C. Koningsberger, P. Kunkeler, H. van Bekkum, A.P.M. Kentgens, *J. Am. Chem. Soc.* 122 (2000) 12842–12847.
- [40] A.E.W. Beers, J.A. van Bokhoven, K.M. de Lathouder, F. Kapteijn, J.A. Moulijn, *J. Catal.* 218 (2003) 239–248.
- [41] P. Bodart, J.B. Nagy, G. Debras, Z. Gabelica, P.A. Jacobs, *J. Phys. Chem.* 90 (1986) 5183–5190.
- [42] J.L. Motz, H. Heinichen, W.F. Hölderich, *J. Mol. Catal. A* 136 (1998) 175–184.
- [43] A. Omegna, M. Haouas, A. Kogelbauer, R. Prins, *Microporous Mesoporous Mater.* 46 (2001) 177–184.
- [44] B. Sieve, S. Sportouch, X.Z. Chen, J.A. Cowen, P. Brazis, C.R. Kannewurf, V. Papaefthymiou, M.G. Kanatzidis, *Chem. Mater.* 13 (2001) 273–283.
- [45] T. Fujii, F.M.F. de Groot, G.A. Sawatzky, F.C. Voigt, T. Hibma, K. Okada, *Phys. Rev. B* 59 (1999) 3195–3202.
- [46] P. Graat, M.A.J. Somers, *Surf. Interface Anal.* 26 (1998) 773–782.
- [47] G. Qi, R.T. Yang, *Appl. Catal. A* 287 (2005) 25–33.
- [48] P. Singh, D.M. Mott, S. Maenosono, *ChemPhysChem* 14 (2013) 3278–3283.
- [49] A.P. Grosvenor, B.A. Kobe, M.C. Biesinger, N.S. McIntyre, *Surf. Interface Anal.* 36 (2004) 1564–1574.
- [50] G. Qi, R.T. Yang, *Appl. Catal. B: Environ.* 60 (2005) 13–22.
- [51] P. Burroughs, A. Hamnett, A.F. Orchard, G. Thornton, *J. Chem. Soc. Dalton Trans.* (1976) 1686–1698.
- [52] E.J.M. Hensen, Q. Zhu, M.M.R.M. Hendrix, A.R. Overweg, P.J. Kooyman, M.V. Sychev, R.A. van Santen, *J. Catal.* 221 (2004) 560–574.
- [53] O.A. Anunziata, A.R. Beltramone, Z. Juric, L.B. Pierella, F.G. Requejo, *Appl. Catal. A* 264 (2004) 93–101.
- [54] T. Pirmohamed, J.M. Dowding, S. Singh, B. Wasserman, E. Heckert, A.S. Karakoti, J.E.S. King, S. Seal, W.T. Self, *Chem. Commun.* 46 (2010) 2736–2738.
- [55] J.Z. Shyu, W.H. Weber, H.S. Gandhi, *J. Phys. Chem.* 92 (1988) 4964–4970.
- [56] H.S. Roh, K.W. Jun, W.S. Dong, J.S. Chang, S.E. Park, Y. Joe, *J. Mol. Catal. A* 181 (2002) 137–142.
- [57] R. Qu, X. Gao, K. Cen, J. Li, *Appl. Catal. B* 142–143 (2013) 290–297.
- [58] Z. Liu, S. Zhang, J. Li, L. Ma, *Appl. Catal. B* 144 (2014) 90–95.
- [59] M. Schwidder, M.S. Kumar, K. Klementiev, M.M. Pohl, A. Bruckner, W. Grunert, *J. Catal.* 231 (2005) 314–330.
- [60] W.H. Chen, H.H. Ko, A. Sakthivel, S.J. Huang, S.H. Liu, A.Y. Lo, T.C. Tsai, S.B. Liu, *Catal. Today* 116 (2006) 111–120.
- [61] R.J. Gorte, *Catal. Lett.* 62 (1999) 1–13.
- [62] S.S.R. Putluru, A. Riisager, R. Fehrmann, *Appl. Catal. B* 101 (2011) 183–188.
- [63] N.Y. Topsøe, K. Pedersen, E.G. Derouane, *J. Catal.* 70 (1981) 41–52.
- [64] A.C. Akah, G. Nkeng, A.A. Garforth, *Appl. Catal. B* 74 (2007) 34–39.
- [65] C.V. Hidalgo, H. Itoh, T. Hattori, M. Niwa, Y. Murakami, *J. Catal.* 85 (1984) 362–369.
- [66] A.V. Salker, W. Weisweiler, *Appl. Catal. A* 203 (2000) 221–229.
- [67] J. Gu, Y. Wu, Y. Jin, J. Wang, *J. Porous Mater.* 20 (2013) 7–13.
- [68] R. Buzzoni, S. Bordiga, G. Ricciardi, C. Lamberti, A. Zecchina, G. Bellussi, *Langmuir* 12 (1996) 930–940.
- [69] G. Busca, *Phys. Chem. Chem. Phys.* 1 (1999) 723–736.
- [70] O.M. Busch, W. Brijoux, S. Thomson, F. Schüth, *J. Catal.* 222 (2004) 174–179.
- [71] T.R. Hughes, H.M. White, *J. Phys. Chem.* 71 (1967) 2192–2201.
- [72] P.A. Jacobs, C.F. Heylen, *J. Catal.* 34 (1974) 267–274.
- [73] E. Sellia, L. Forni, *Microporous Mesoporous Mater.* 31 (1999) 129–140.